Behavior of settling particles in homogeneous shear turbulence

Seulgi Lee [*]
Department of Mechanical Engineering, Yonsei University, Seoul 03722, Korea

Changhoon Lee[†]
*Department of Computational Science and Engineering and Department of Mechanical Engineering,
Yonsei University, Seoul 03722, Korea*

In this study, particle-laden shear turbulence is investigated by performing direct numerical simulation under a point-particle approximation for spherical heavy particles with a diameter smaller than the Kolmogorov length scale of the flow. The ranges of the Stokes number and gravity factor considered in our study are $St = 0.1, 0.5, 1, 5,$ and 10 and $W(= v_t/v_\eta) = 0, 10, 20, 30,$ and 40, respectively, where v_t and v_η are the terminal velocity and the Kolmogorov velocity scale, respectively. The behavior of settling particles is investigated by introducing a two-dimensional distribution function to quantify the anisotropic clustering. A principal component analysis of the two-dimensional distribution evidently indicates that the preferential orientation of clustering at different scales is identified well. Small-scale clustering displays a multifractal nature with an explicit angular distribution.

I. INTRODUCTION

Particle-laden turbulent flows are frequently observed in nature and various engineering applications, and some examples are droplets in clouds, planktons in an ocean, sedimenting particles in a river, particles in chemical reactors, and fuel droplets in an internal combustion engine [1–4]. Therefore numerous studies on the transport of particles in a turbulent environment have been conducted experimentally and numerically. Particularly, the clustering of inertial particles, which is one of their most prominent phenomena occurring in turbulence, has been identified for particles whose timescales are comparable to the Kolmogorov timescale of the background turbulence $(St \leqslant 1)$ [5–9]. The main mechanism of this phenomenon, also known as preferential concentration, is the centrifuge effect of the inertial particles around rotating structures of turbulence. Therefore most inertial particles are accumulated in the region where the rotational motion of the fluid is weak and the straining motion is relatively strong. For particles with $St > 1$, mechanisms other than the centrifuge effect have been proposed to explain the appearance of particle clusters of multiscale nature. Goto and Vassilicos [10], Chen *et al.* [11] observed in two-dimensional turbulence that inertial particles tend to stick preferentially to the zero-acceleration point of the background flow. In particular, Goto and Vassilicos [12] extended this idea to three-dimensional turbulence and revealed a sweep-stick mechanism of preferential concentration for Stokes numbers above unity. However, in consideration of the settling motion of inertial particles due to gravity, a new type of preferential accumulation in columnar structures was observed in isotropic turbulence [13,14]. Because gravitational settling is inevitable in real flows, the effect of gravity should be considered

---

*sg.lee@yonsei.ac.kr
†Corresponding author: clee@yonsei.ac.kr

for developing an appropriate understanding of the behavior of particles in real scenarios. For example, the clustering of sedimenting droplets in clouds can influence the droplet adhesion by affecting the collision efficiency [9,15–18].

However, the behavior of inertial particles in an anisotropic turbulent environment is remarkably different from that in isotropic turbulence. Therefore studies on the behavior of inertial particles in anisotropic flows have also been actively conducted theoretically, experimentally, and numerically [19–27]. However, most of these studies considered inhomogeneous shear flows, such as jets, mixing layers, and channel flows, which present inhomogeneous distributions of the mean velocity and turbulent stresses. A similar preferential accumulation is observed in the center region of a channel where the flow is nearly homogeneous. Furthermore, owing to the inhomogeneity of turbulence, another type of migration of particles, known as turbophoresis, occurs, which causes, for example, accumulation of inertial particles in the near-wall region. Although the effect of gravity on the behavior of inertial particles in these flows has been studied [28–31], it is difficult to determine the fundamental mechanism of the clustering found in these flows owing to the combined effect of the inhomogeneity and anisotropy of turbulence.

To study the effect of anisotropy of turbulence on the behavior of inertial particles, a homogeneous shear turbulence (HST) is an ideal flow to investigate. HST without laden particles has been actively studied experimentally and numerically for a long time [32–40]. To develop a model of shear turbulence under an unbounded condition, most of these studies focused on a transient shear turbulence. Both experimental and numerical studies demonstrated that the integral length scale and the turbulent kinetic energy increase with time. Pumir [41] suggested that the finite size of the domain would prevent the increase to a large scale, unlike in an unbounded shear turbulence. We actually confirmed numerically that the production and dissipation of a turbulence are balanced in a confined space, which allows a statistically steady state. Similar features were also found in the experiments by Shen and Warhaft [42].

Several studies have been performed to analyze the behavior of particles in an HST. The behaviors of suspended particles in a transient shear turbulence were investigated in [43,44]. Ahmed and Elghobashi [43] studied particle dispersion in an HST at various shear numbers, particle response times, and directions of gravity. They found that in the absence of gravity, the particle dispersion in the streamwise direction is at least one order of magnitude larger than those in the other directions owing to the mean advection. In comparison, on application of gravity, the particle dispersion in all directions decreases. It was also confirmed that the preferential accumulation is maximized when the Kolmogorov timescale and the particle response time are of the same order of magnitude. Shotorban and Balachandar [44] also discussed preferential accumulation; specifically, particles were most concentrated in the stream direction and not in the stress-stream direction. Gualtieri *et al.* [45] investigated the behavior of particles for various Stokes numbers in a statistically steady shear turbulence. They evaluated the anisotropy properties by introducing an angular distribution function. The results provided evidence that depending on the Stokes number, anisotropic clustering may occur even in the range of the scales in which the carrier phase velocity field is already recovering the isotropy. Moreover, analysis of particle behavior in a two-way coupling regime has been conducted [46–48]. However, the long-term clustering behavior of settling particles in HST is still not fully studied. Therefore, in this study, we investigate the clustering behavior of particles in a statistically stationary shear turbulence under the effect of gravity. First we observe the mean motion of particles in HST before discussion on particle clustering because the enhanced particle settling in turbulence is well known to be caused by the preferential sweeping mechanism [49,50]. Then we quantitatively present the properties of anisotropic clustering for various inertial particles and gravitational magnitudes and confirm whether small-scale clustering exhibits a fractal nature. For this purpose various statistics are presented, and in particular, we address a two-dimensional distribution function (2DF) to characterize the anisotropic clustering.

The remainder of this paper is organized as follows. In Sec. II we describe the numerical procedures for the simulation of particle-laden shear turbulence in a confined computational box. The simulation results are discussed in detail in Sec. III. The conclusions are drawn in Sec. IV.

TABLE I. Time-averaged turbulence statistics. $\text{Re}_\lambda = q^2\sqrt{5/3\nu_f\epsilon}$, $S^* = Sq^2/\epsilon$, $L_s = \sqrt{\epsilon/S^3}$, shear length scale, and $q^2 = \langle u_i' u_i' \rangle$. η and τ_η are the Kolmogorov length and the timescale, respectively.

Re_λ	S^*	η	τ_η	ϵ	L_s	$\langle u_1'^2 \rangle / q^2$	$\langle u_2'^2 \rangle / q^2$	$\langle u_3'^2 \rangle / q^2$	$\langle u_1' u_2' \rangle / q^2$
68	7	0.0358	0.0869	2.40781	0.76671	0.5593	0.2406	0.2301	−0.1493

II. NUMERICAL PROCEDURES

A. Homogeneous shear turbulence

To study the behavior of particles laden in an HST, first the turbulence should be appropriately established. In this section we briefly describe the simulation of an HST. The governing equations for an incompressible flow are Navier-Stokes and continuity equations,

$$\frac{\partial u_i}{\partial t} + u_j \frac{\partial u_i}{\partial x_j} = -\frac{1}{\rho_f} \frac{\partial p}{\partial x_i} + \nu_f \frac{\partial^2 u_i}{\partial x_j \partial x_j}, \tag{1}$$

$$\frac{\partial u_i}{\partial x_i} = 0, \tag{2}$$

where t is the time, u_i is the velocity of the fluid in the x_i direction, and x_1 (x), x_2 (y), and x_3 (z) denote the streamwise, cross-streamwise, and spanwise directions, respectively. Here p, ρ_f, and ν_f are the pressure, density of the fluid, and kinematic viscosity of the fluid, respectively. We consider a simple shear flow with a uniform shear rate, S; therefore the velocity field u_i is decomposed into a sum of the mean shear flow, $U_i = Sx_2\delta_{i1}$, and a fluctuating velocity u_i'. Using this decomposition, one can rewrite the Navier-Stokes equation and continuity equations for the fluctuating quantities as

$$\frac{\partial u_i'}{\partial t} + u_j' \frac{\partial u_i'}{\partial x_j} + Sx_2 \frac{\partial u_i'}{\partial x_1} + S\delta_{i1}u_2' = -\frac{1}{\rho_f} \frac{\partial p}{\partial x_i} + \nu_f \frac{\partial^2 u_i'}{\partial x_j \partial x_j}, \tag{3}$$

$$\frac{\partial u_i'}{\partial x_i} = 0. \tag{4}$$

The presence of mean velocity due to uniform shear does not allow typical periodic conditions in all directions. In the shear direction (y), the so-called shear-periodic condition is satisfied. The shear-periodic boundary condition for a quantity of interest $f(x, y, z, t)$ is prescribed by

$$f(x, y + L_y, z, t) = f(x - SL_y t, y, z, t), \tag{5}$$

where L_y is the domain size in the y direction, indicating that the computation domain stays deformed in time.

To implement the shear-periodic condition for the fluctuation quantities, we adopted the algorithm of Brucker *et al.* [51], which works directly in a fixed orthogonal frame. The drawback of this algorithm is that the wave numbers in the shear direction continue to increase, which limits the grid resolution [52]. To resolve this we introduced the remeshing process proposed by Rogallo [53]. Using the combination of the above two algorithms, we could maintain a statistically stationary shear turbulence for a long time in the orthogonal frame without a physical frame deformed by mean shear.

Equations (3) and (4) are solved by a pseudospectral method under the shear-periodic boundary condition, and a third-order Runge-Kutta scheme is adopted for time advancement. The orthogonal computation domain is $[0, 2\pi] \times [-\pi, \pi] \times [0, 2\pi]$ with a resolution of $128 \times 128 \times 128$. Time-averaged turbulence statistics are listed in Table I: the Taylor-scale Reynolds number, $\text{Re}_\lambda (= u'\lambda/\nu_f = q^2\sqrt{5/3\nu_f\epsilon}) = 68$, and the nondimensional shear parameter, $Sq^2/\epsilon = 7$. Here
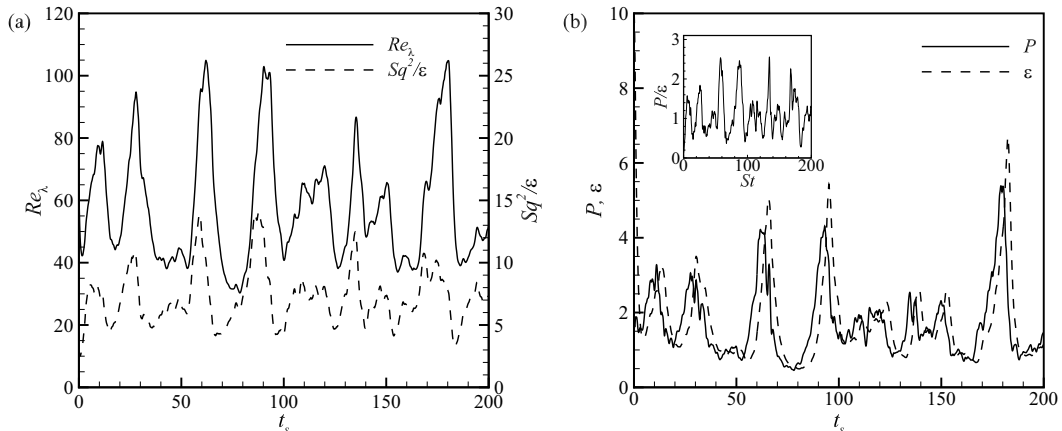
FIG. 1. Statistics of flows in HST: (a) Reynolds number Re_λ and shear parameter Sq^2/ϵ; (b) dissipation rate ϵ and production $P = -S\langle u_1 u_2 \rangle$ over 200 shear timescales, $t_s = S \times t = 200$. Inset in (b) shows ratio of production and dissipation.

$q^2 = \langle u_i' u_i' \rangle$, and ϵ is the turbulence dissipation rate. It is noted that the anisotropy of shear turbulence is represented by $\langle u_1'^2 \rangle > \langle u_2'^2 \rangle \simeq \langle u_3'^2 \rangle > |\langle u_1' u_2' \rangle|$.

Temporal variation in statistical quantities over a long period $S \times t = 200$, such as Reynolds number, shear parameter, dissipation rate, and production $P(= -S\langle u_1' u_2' \rangle)$, is shown in Fig. 1, demonstrating that these statistics widely oscillate while maintaining the stationarity over a very long time. The ratio of the production and dissipation rates presented in the inset of Fig. 1(b) clearly indicates that the simulated turbulence is indeed statistically stationary. It is noticeable that the dissipation rate lags behind the production in the temporal variation, as displayed in Fig. 1(b). In this study the sufficiently developed HST at $S \times t = 200$ is used for the initial field to investigate the behavior of settling particles.

B. Motion of particles in HST

The particles considered in this study are small, heavy, and spherical. The diameter of a particle is much smaller than the Kolmogorov length scale, (i.e., $d_p/\eta \ll 1$); therefore a point-particle approach can be used, and the feedback force is ignored (one-way interaction). Stokes drag is adopted because the particle density is much higher than the fluid density (i.e., $\rho_p/\rho_f \gg 1$). Accordingly, the equations of motion for particle position x_i^p and particle velocity v_i are expressed as

$$\frac{dx_i^p}{dt} = v_i, \tag{6}$$

$$\frac{dv_i}{dt} = \frac{1}{\tau_p}(u_i - v_i) - g\delta_{i2}, \tag{7}$$

where u_i is the fluid velocity at the particle position $[x_1^p(t), x_2^p(t), x_3^p(t)]$, g is the gravitational acceleration, and $\tau_p = \frac{\rho_p d_p^2}{18\nu_f \rho_f C}$ is the local particle response time, where the Reynolds-number-dependent numerical factor $C = 1 + 0.15\text{Re}_p^{0.687}$ is considered, which is valid in the range of $\text{Re}_p < 800$. The particle Reynolds number, i.e., $\text{Re}_p = |u_i - v_i|d_p/\nu_f$, is not small when the Stokes number is large and gravity is strong. We observed that $0.0001 < \text{Re}_p < 50$ in all cases considered in the

TABLE II. Cases considered in this study. Averaged particle Reynolds number and the ratio of particle diameter to the Kolmogorov length scale for various Stokes numbers and gravity factors. Density ratio of a particle (copper) to fluid (air) is 7450.

	St = 0.1		St = 0.5		St = 1		St = 5		St = 10	
W	Re_p	d_p/η	Re_p	d_p/η	Re_p	d_p/η	Re_p	d_p/η	Re_p	d_p/η
0	3.54×10^{-4}	0.0157	6.07×10^{-3}	0.0351	0.0114	0.0497	0.261	0.114	0.524	0.164
10	0.648	0.0165	1.27	0.0380	2.13	0.0555	5.14	0.134	11.4	0.210
20	1.30	0.0170	2.52	0.0397	4.20	0.0587	9.86	0.145	22.7	0.237
30	1.94	0.0174	3.77	0.0411	6.25	0.0613	14.7	0.155	33.9	0.257
40	2.59	0.0178	5.02	0.0423	8.31	0.0635	19.5	0.163	45.2	0.274

present study, as listed in Table II. Using the decomposition of the particle velocity, $v_i = v_i' + Sx_2^p\delta_{i1}$, Eqs. (6) and (7) can be rewritten,

$$\frac{dx_i^p}{dt} = v_i' + Sx_2^p\delta_{i1}, \tag{8}$$

$$\frac{dv_i'}{dt} = \frac{1}{\tau_p}(u_i' - v_i') - g\delta_{i2} - S\frac{dx_2^p}{dt}\delta_{i1}. \tag{9}$$

For the interpolation of the fluid velocity at the position of a particle, a four-point Hermite interpolation scheme is applied in all three directions in the orthogonal grid [54,55]. Particular attention is needed to apply the interpolation scheme to particles near the top or bottom boundary to satisfy the shear-periodic condition [56]. To illustrate this we consider two particles marked as blue stars in the 4×4 grid points shown in Fig. 2. Flow data depicted as filled squares are obtained by simulation. Open squares denote the positions satisfying the shear-periodic condition. The values in the x_1 direction can be used directly because they satisfy the ordinary periodic conditions. However, the values in the x_2 direction must be shifted to Cartesian coordinates (red circles) according to the shear-periodic condition. If a particle is at the upper boundary, as shown in the left side in Fig. 2(a), interpolation in two planes is required. Here the data at $ABCD$ and $EFGH$ are used to obtain the data at $A'B'C'D'$ and $E'F'G'H'$, respectively. Similarly, if a particle is at the bottom, as shown in the right side in Fig. 2(b), the value at the particle position should be interpolated using the value
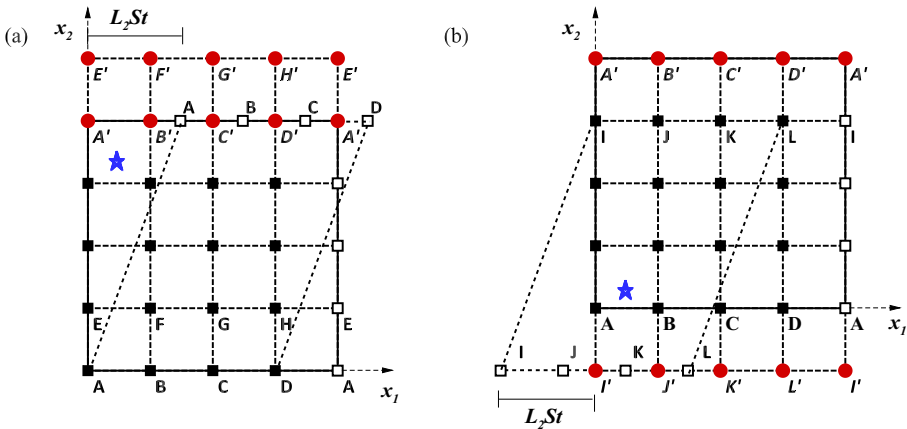
FIG. 2. Schematics showing method to interpolate data for particles located near (a) the top boundary and (b) the bottom boundary to satisfy the shear-periodic condition.

obtained by the interpolated data of $I'J'K'L'$ using the data at $IJKL$. The time integration for Eqs. (6) and (7) is conducted using the third-order Runge-Kutta scheme [57,58].

The particle dynamics are determined by the Stokes number St and the gravity factor W, defined as St $= \overline{\tau_p}/\tau_\eta$ and $W = g\overline{\tau_p}/v_\eta$, respectively, where $\overline{\tau_p} = 1/T \int \tau_p dt$. v_η is the Kolmogorov velocity scale. Froude number, Fr $= v_\eta/(g\tau_\eta) = $ St$/W$, can be used alternatively. In this study the behavior of 160 000 particles for the period of $S \times t = 150$ is investigated for 25 cases (5 Stokes numbers×5 gravity factors). The considered values of the Stokes number and the gravity factor are St $= 0.1, 0.5, 1, 5,$ and 10 and $W = 0, 10, 20, 30,$ and 40, respectively. All cases considered in the present study are listed in Table II in terms of the particle Reynolds number and the particle diameter relative to the Kolmogorov length scale, validating the point-particle approach.

III. RESULTS AND DISCUSSION

The visual results of the particle distribution for various Stokes numbers and gravity factors in the vertical x-y plane, with the y axis denoting the negative gravitational direction, are shown in Fig. 3 to provide an overall picture. Here the colored contour levels represent the magnitude of a vorticity component normal to the plane. In Fig. 3 the cases are arranged such that the Stokes number increases from top to bottom for St $= 0.1, 0.5, 1, 5,$ and 10, and the gravity factor increases from left to right for $W = 0, 10,$ and 30. First we observe that the behavior of the particles in the HST in the absence of gravity is similar to that in a homogeneous isotropic turbulence in that the maximum clustering of the particles occurs at St $= 1$ (see the left column in Fig. 3). However, the pattern of clustering at St $= 1$ indicates that there exists a preferential direction in the particle clusters owing to the mean shear motion of the fluid.

When particle settling is considered, more diverse patterns of clustering are observable compared to the cases without the gravitation effect. When St $\ll 1$, no clustering is found, whereas as St approaches 1 and further increases, various patterns of clustering are remarkably visible. In all cases presenting clustering, the effect of the mean shear motion is reflected on the slanted pattern of clustering to different extents. These patterns, particularly for St ~ 1 and $W = 10$ and 30, are somewhat similar to the pattern aligned with the gravitational direction found in the settling particles in an isotropic turbulence [14]. Owing to the presence of shear, the pattern of clustering seems to be relatively more complex. Another interesting finding is that the particles with St $= 5$ and 10, which did not display any pronounced pattern in the absence of gravity, exhibit a very strong linear pattern, which has never been observed in any particle-laden turbulence.

In the following sections we discuss the investigation of the behavior of the particles, analyzing various statistical quantities in detail. First, the effect of shear turbulence is examined by comparing the terminal and slip velocities in the x and y directions in a turbulence-free shear flow with the averaged velocity of the particles suspended in the HST. We also compare the analytic solutions of the terminal trajectories in the turbulence-free shear flow with those of the ensemble-averaged trajectories of the particles in the HST. The details are covered in Sec. III A. Next, the clustering of particles is discussed in Secs. III B and III C in terms of the closest distance between particles and a two-dimensional pair correlation function called 2DF, respectively. Finally, in Sec. III D we discuss the multifractal nature of the particle clusters as indicated by 2DF.

A. Mean statistics of particle motion

This section initially presents the mean statistics of particle motion, such as the settling velocity, horizontal slip velocity, and mean particle trajectory. After a certain transient period, owing to the initial random distribution of the particles the average velocity of the particles reaches a steady value asymptotically over time. In an HST, the settling particles can eventually present mean settling and horizontal slip velocities. From an ensemble average of Eq. (9), as $t \to \infty$,

$$\langle v_i' \rangle = \langle u_i'(x_i^p) \rangle - \overline{\tau_p} g \delta_{i2} - S\overline{\tau_p}\langle v_2' \rangle \delta_{i1}, \tag{10}$$
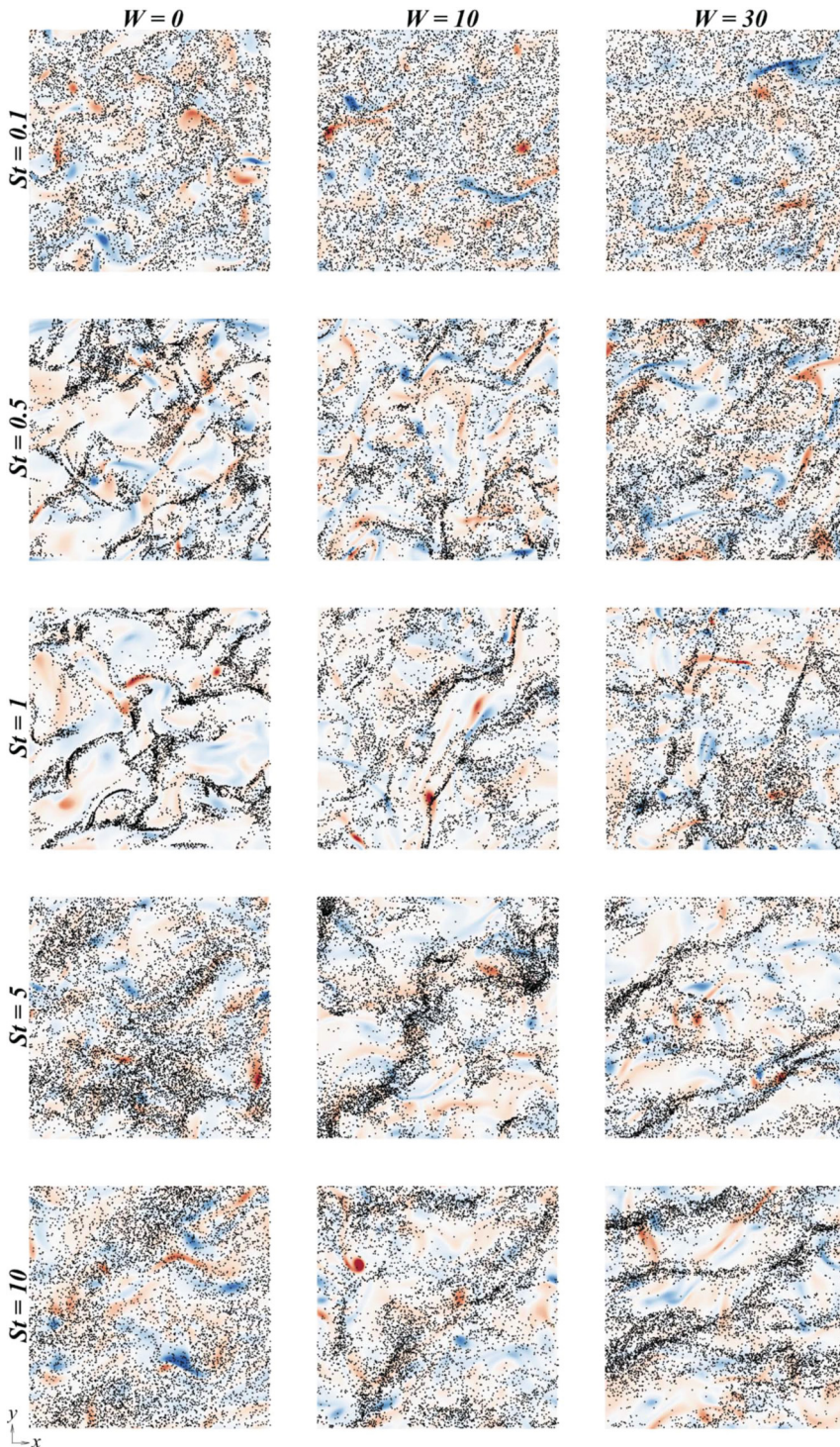
FIG. 3. Particle distribution for various Stokes numbers and gravity factors. Gravity acts in vertical direction. Colored contour denotes spanwise vorticity. From top to bottom, St = 0.1, 0.5, 1, 5, and 10, respectively. From left to right, $W = 0$, 10, and 30, respectively.
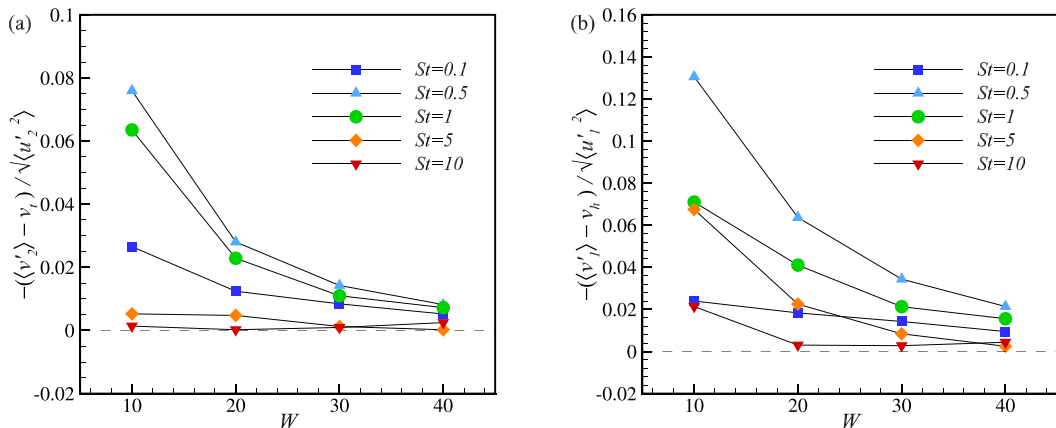
FIG. 4. (a) Plots of difference between mean settling velocity and terminal velocity and (b) difference between mean horizontal particle velocity and horizontal slip velocity for various Stokes numbers and gravity factors.

where the second term on the right side is the terminal velocity in a stationary fluid, $v_t = -\overline{\tau_p}g$, and the third term is the horizontal slip velocity of the particles relative to that in the turbulence-free shear flow, $v_h = S\overline{\tau_p}^2 g$. The effect of turbulence is reflected on the first term. The average settling velocity of the particles relative to v_t and the average slip velocity of the particles relative to v_h are shown in Fig. 4 as a function of Stokes number and the gravity factor. When normalized by $\langle u_2'^2 \rangle^{1/2}$, which is the average vertical velocity of the fluid at the particle position, the settling velocities for all Stokes numbers are higher than the terminal velocity in the stationary fluid, and the difference monotonically decreases with the gravity factor. At a given gravity factor, this difference is maximum at St = 0.5, and when $W = 10$, it is 8%. Wang and Maxey [49] investigated the settling velocity under a weak gravity ($W \leqslant 4$) for St < 1 in a homogeneous isotropic turbulence and found that the settling velocity is higher than the terminal velocity. This is owing to the preferential sweeping of the particles in a downward-moving fluid, and the difference between the settling and terminal velocities reaches a maximum in the interval $1.5 < W < 2.5$ and then decreases. However, in our study we focused on a comparatively wider range of the gravity factor; we did not identify the value of the gravity factor showing the local maximum difference. Furthermore, their Reynolds number is quite small ($R_\lambda = 31$), and thus their observation is not directly generalized to a high-Reynolds-number flow. Recently, Ireland et $al.$ [59] discussed the settling velocity extending the range of Reynolds numbers for $0 \leqslant$ St $\leqslant 3$ and Fr = 0.025. They observed that the settling velocity of inertial particles with St > 1 is not affected by turbulence at $R_\lambda = 90$, consistent with our results. Moreover, they revealed that the mean settling velocity is independent of R_λ for St < 0.1, suggesting that in this limit it is determined entirely by the small-scale turbulence and is a stronger function of the Reynolds number at higher St. This leads to a consideration of multiscale preferential sweeping by Tom and Bragg [50], in which they observed that increasingly larger scales contribute to the enhanced particle settling due to the turbulence as St increases. Furthermore, they confirmed another prediction of theory that the vertical component of mean fluid velocity at particle position, $\langle u_2'(x_2^p) \rangle$, is affected by an increasingly larger scale for a given St as Fr decreases (W increases). This could provide an explanation for increased cluster size in the presence of gravity that will be confirmed in Sec. III C.

The horizontal slip velocity relative to that in a turbulence-free shear flow, as shown in Fig. 4(b), exhibits similar dependency on the Stokes number and the gravity factor. When St = 0.5, the difference in the slip velocity normalized by $\langle u_1'^2 \rangle^{1/2}$ reaches 13% for $W = 10$. Note that for particles with St = 5 or 10, a non-negligible difference is observed, unlike for the settling velocity.
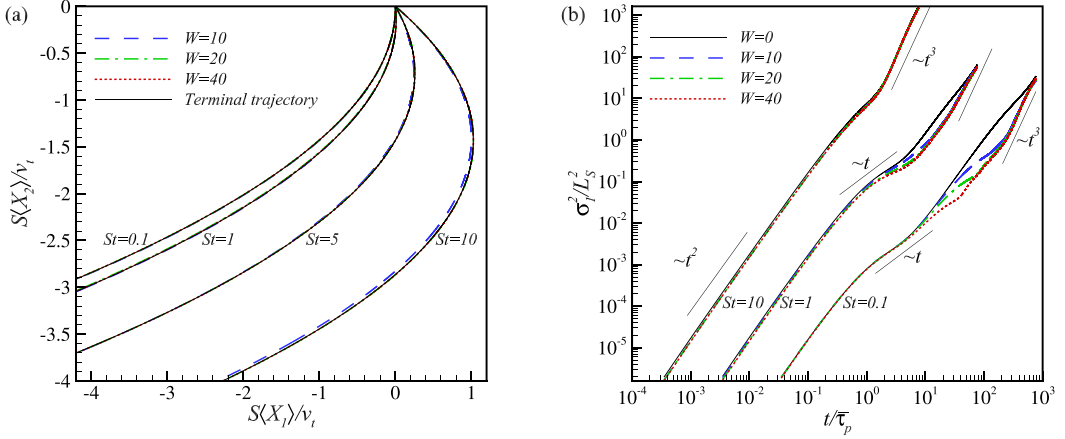
FIG. 5. (a) Plots of particle trajectory for various Stokes numbers and gravity factors and (b) dispersion relative to terminal trajectory. Average particle trajectory is normalized by settling velocity and shear rate. Terminal trajectories for turbulence-free shear flow are expressed as $x_1^t = S\overline{\tau}_p^2 gt - \frac{1}{2}S\overline{\tau}_p gt^2$ and $x_2^t = -\overline{\tau}_p gt$. Dispersions are displayed for St = 0.1, 1, and 10.

The existence of settling and horizontal slip velocities warrants the consideration of the particle trajectories. First, an analytical solution of the terminal trajectory of a particle in the turbulence-free shear flow can be obtained by an integral of Eq. (8), where the terminal value of v_i' for a turbulence-free flow is expressed by $v_2' = -\overline{\tau}_p g$ and $v_1' = S\overline{\tau}_p^2 g$, and the second term on the right side can be replaced by a function of time as $x_2^p = v_2't = -\overline{\tau}_p gt$. Thus the terminal trajectory in a turbulence-free shear flow is given by

$$x_i^t(t) = \left(S\overline{\tau}_p^2 gt - \tfrac{1}{2}S\overline{\tau}_p gt^2\right)\delta_{i1} - \overline{\tau}_p gt\delta_{i2}, \tag{11}$$

indicating that the particles are settling while forming a parabolic trajectory. In the HST, the ensemble-averaged particle trajectory $\langle X_i \rangle$ can be obtained by the averaged displacement of the particles relative to each initial position,

$$X_i(t) = x_i^p(t_0 + t) - x_i^p(t_0) - S\delta_{i1}x_2^p(t_0)t, \tag{12}$$

where t_0 is chosen to avoid the initial transient period due to the random distribution of the particles. The ensemble-averaged trajectories normalized by v_t/S are displayed for different Stokes numbers and gravity factors in Fig. 5(a) along with the terminal trajectory in the turbulence-free shear flow given by Eq. (11) for comparison. For all cases the ensemble-averaged particle trajectory is almost identical to the terminal trajectory in the turbulence-free shear flow, although a slight deviation is observed for St = 10. It appears that turbulence does not play any role in determining the mean particle trajectory, and thus Eq. (11) is a good estimator of the particle trajectory in the HST for the range of parameters considered in the present study.

Next the dispersion of particles relative to the average trajectory was investigated. Particularly, the dispersion of the particles in the streamwise direction given by $\sigma^2(t) = \langle (X_1(t) - x_1^t(t))^2 \rangle$ is shown in Fig. 5(b), illustrating the time development of σ^2 on a log scale for all the Stokes numbers. The x axis is normalized by the particle response timescale $\overline{\tau}_p$, and the y axis is normalized by the shear scale L_s. A typical ballistic-to-diffusion transition, $(t^2 \to t^1)$, is followed by shear diffusion (t^3) [60]. For St = 10 the diffusion behavior is not observed, whereas for St = 0.1 or 1, the shear diffusion is found for large gravity factors.
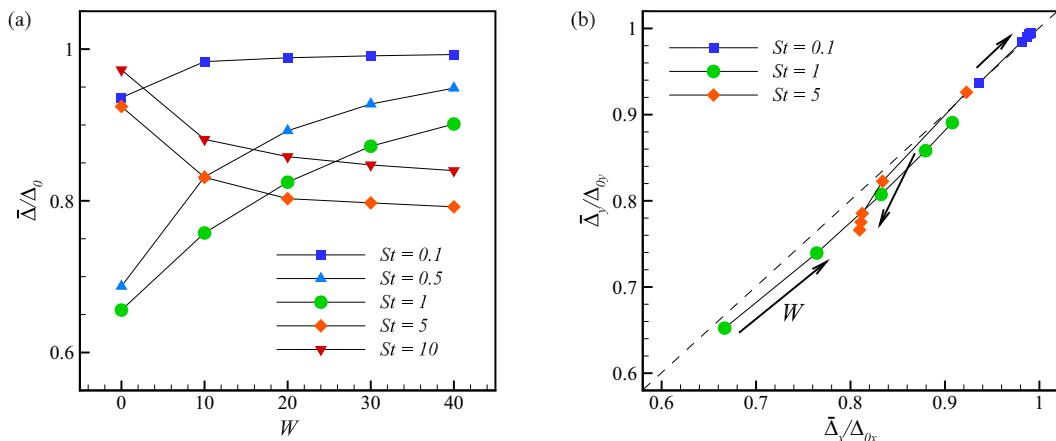
FIG. 6. Plots of average closest distances. (a) Drawn with gravity factor for St = 0.1, 0.5, 1, 5, and 10. (b) Drawn with average closest distance in each direction. The average closest distance is normalized by the corresponding value for a random distribution of the same number of particles in the same domain so that values smaller than 1 indicate clustering.

B. Clustering of particles: Closest distance

In this section the statistics of the closest distance between particles are discussed to quantify the clustering phenomenon. These statistics were used for isotropic turbulence by Park and Lee [14] and are a simple tool to assess the clustering of particles. The average closest distance Δ is defined by

$$\Delta = \langle \min_{k \neq j} |x_{i,j}^p - x_{i,k}^p| \rangle, \tag{13}$$

where $x_{i,j}^p$ denotes the position of the jth particle, and the bracket denotes averaging over all the particles. Figure 6 shows the average closest distances normalized by Δ_0, which is the corresponding value for a random distribution of the same number of particles, for various Stokes numbers. The bar above δ indicates the temporal average. $\bar{\Delta}/\Delta_0 = 1$ suggests a uniform distribution, and $\bar{\Delta}/\Delta_0$ is indicative of when the clustering of particles occurs as $\bar{\Delta}/\Delta_0 < 1$.

In the absence of gravity, the clustering of particles occurs when St = 0.5 and 1 and is maximized at $St = 1$, whereas no such clustering is observed when St $\gg$ 1, which is similar to the typical behavior observed in a homogeneous isotropic turbulence. On the other hand, as the gravitational strength increases, the clustering behavior drastically changes. When St $\leqslant$ 1, the clustering is rapidly weakened as W increases. However, when St > 1, the particles tend to cluster as W increases, although the pattern of the clusters is different from the case with St = 1 in the absence of gravity, as shown in Fig. 3.

The clustering behavior of particles for St $\leqslant$ 1 in the absence of gravity can be well explained by the centrifuge effect. As the gravity factor increases, however, particles settle faster. Then the chance of interaction between the settling particles and vortical structures gets reduced, resulting in weakening of clustering. For St $\gg$ 1, however, several experimental and numerical observations provided evidence showing large-scale clustering, regardless of gravity [61–63]. This was explained by the sweep-stick mechanism introduced by Goto and Vassilicos [12], that particles tend to stick preferentially to the zero-acceleration point of fluid. Since the closest distance is the statistics characterizing small-scale clustering, it cannot capture large-scale clustering. However, the large-scale clustering was clearly observed for St $\gg$ 1 in Fig. 3. It appears that as gravity gets stronger, this large-scale clustering becomes more pronounced.

The small-scale structure of clustering can be investigated by the components of the closest distance [14]. The horizontal and vertical components of the averaged closest distance, $\bar{\Delta}_x$ vs $\bar{\Delta}_y$, are presented in Fig. 6(b). However, in most cases, $\bar{\Delta}_y$ is slightly smaller than $\bar{\Delta}_x$. In the absence of gravity, $\bar{\Delta}_x$ is almost the same as $\bar{\Delta}_y$. Although W increases, the difference between them does not change significantly. The anisotropic nature of clustering observed in Fig. 3 requires more appropriate analysis, which will be described in the next section.

C. Anisotropic clustering of particles: 2DF

A radial distribution function (RDF) has been used to analyze the relative distribution of particles. However, an RDF is an unsuitable tool to determine the anisotropic clustering of particles. Gualtieri *et al.* [45] considered the angular distribution function (ADF) in HST by extending the RDF. In the current study we propose simpler and more visible statistics. With the particle number density defined by $n(x_i, t) = \sum_j \delta[x_i - x_{i,j}^p(t)]$, the pair correlation of particles $\langle n(x_i, t)n(x_i + r_i, t)\rangle$ defines a general three-dimensional distribution function,

$$g(x_i, r_i, t) = \frac{\langle n(x_i, t)n(x_i + r_i, t)\rangle}{\langle n(x_i, t)\rangle\langle n(x_i + r_i, t)\rangle}. \tag{14}$$

Under the homogeneous isotropic stationary condition, $g(x_i, r_i, t)$ reduces to RDF $g(r)$ with $r = (r_i r_i)^{1/2}$:

$$g(r) = \frac{\langle n(0)n(r)\rangle}{\langle n\rangle^2}. \tag{15}$$

Extending the statistics, we consider the pair correlation function of particles in two dimensions, defined as

$$g(x, y) = \left.\frac{\langle n(0, 0, 0)n(x, y, z)\rangle}{\langle n\rangle^2}\right|_{-0.3\eta < z < +0.3\eta}, \tag{16}$$

which we call the two-dimensional distribution function (2DF). $g(x, y) = 1$ indicates a uniform distribution, whereas $g(x, y) > 1$ or $g(x, y) < 1$ suggests clustering or void, respectively. $g(x, y)$ can provide information on the structure of the anisotropic clustering of particles.

Figure 7 shows the distribution of 2DF for St $= 0.1, 0, 5, 1, 5$, and 10 as the gravity factor increases. The 2DF value is obtained by measuring the distance between all pairs of the particles. Each axis is normalized by the Kolmogorov length scale, η. The contour level represents the value of 2DF. Here the level marked in blue $[g(x, y) = 1.06]$ denotes the structure of the large-scale clustering of particles. In addition, for St $= 0.1$ the domain is enlarged because the structure of particle clustering is small. The first column in Fig. 7 presents 2DF, depending on the Stokes number in the absence of gravity. It is observed that the value of 2DF at the origin, $\langle n^2\rangle/\langle n\rangle^2$, shows a maximum when St $= 1$, implying that the degree of clustering is maximized. The maximum and minimum values of $g(x, y)$ are listed in Table III. The distributions for all the values of the gravity factor indicate that there exists a preferential direction in the patterns of the clusters.

When St $\leqslant 1$, the tendency of particle clustering decreases with increasing gravity factor, as confirmed by the contour level in Fig. 7 and the maximum value at the center (see Table III). Particularly, when $W = 10$, the cluster structure is large and elongated in the slanted direction. When $W > 10$, the size of the structure decreases. When St $= 0.1$, particle clustering appears to be relatively weaker and less affected by gravity. However, when St > 1, particle clustering becomes stronger and more anisotropic with increasing gravity, as depicted in Fig. 7. This can be confirmed by the maximum value of 2DF at the center, as listed in Table III. It is noteworthy that the void region becomes more pronounced near the sides of the elongated cluster structure. These observations indicate that clustering in this parameter range (St > 1 and $W \geqslant 10$) occurs in a large scale, as depicted in Fig. 3, which is remarkably different from the typical clustering, for St $= 1$. Furthermore, the angle of the cluster structure measured from the horizontal direction tends
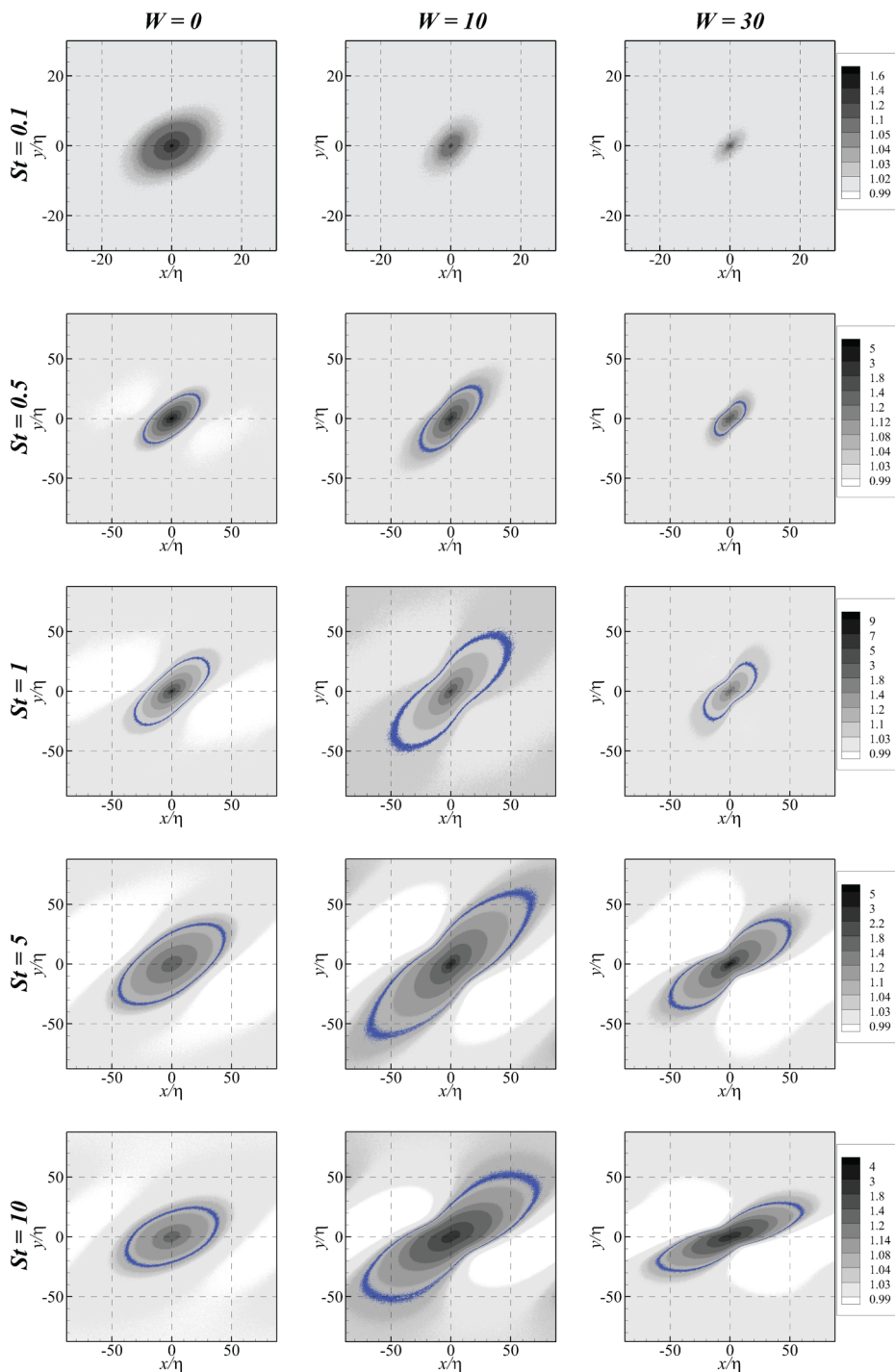
FIG. 7. Two-dimensional distribution function (2DF) for various Stokes numbers and gravity factors. From top to bottom, St = 0.1, 0.5, 1, 5, and 10, respectively. From left to right, $W = 0$, 10, and 30, respectively. The gray-scale contour level represents the 2DF values for the same Stokes number. The blue contour denotes $g(x, y) = 1.06$, and the area inside the blue line is taken as the structure of large-scale clustering. The white region indicates a relatively void region.

TABLE III. Minimum and maximum values of 2DF at various Stokes numbers and gravity factors. The maximum value, which is $\langle n^2 \rangle / \langle n \rangle^2$, is typically found at the origin.

	St = 0.1		St = 0.5		St = 1		St = 5		St = 10	
W	g_{min}	g_{max}	g_{min}	g_{max}	g_{min}	g_{max}	g_{min}	g_{max}	g_{min}	g_{max}
0	0.974	1.70	0.965	16.7	0.953	22.5	0.924	1.91	0.954	1.29
10	0.975	1.16	0.982	5.29	0.993	10.4	0.922	4.50	0.924	3.53
20	0.975	1.14	0.974	2.72	0.972	5.62	0.901	5.69	0.899	4.18
30	0.975	1.12	0.969	1.88	0.973	3.52	0.893	5.94	0.896	4.49
40	0.954	1.09	0.976	1.53	0.976	2.63	0.892	6.15	0.892	4.71

to decrease as the gravity factor increases, which is also noted in the snapshot distribution of the particles in Fig. 3.

For a relatively more quantitative analysis of 2DF, we conduct the principal component analysis (PCA) [64]. Particularly, we use PCA to identify the orientation of the cluster structure in various scales, because PCA can provide principal direction to the particle distribution. Here the principal direction refers to the direction along which the variance of data is the largest. First we define the covariance matrix $C_{ij}(h)$ as a function of the value of the level h in 2DF for a given distribution of particles in two dimensions $x^p_{i,k}$:

$$C_{ij}(h) = \frac{1}{N_p N_q(h)} \sum_k^{N_p} \sum_{l \neq k}^{N_q(h)} \left(x^p_{i,l} - x^p_{i,k} \right) \left(x^p_{j,l} - x^p_{j,k} \right), \quad \text{for } g\left(x^p_{1,l} - x^p_{1,k}, x^p_{2,l} - x^p_{2,k} \right) \geqslant h, \quad (17)$$

where N_p is the total number of particles, and $N_q(h)$ is the number of pairs of particles satisfying the inequality condition in Eq. (17). In two dimensions, $C_{11}(h)$ and $C_{22}(h)$ represent the horizontal and vertical variances, respectively, of the relative distance between a pair of particles satisfying the inequality condition of Eq. (17). $C_{12}(h) (= C_{21}(h))$ indicates the correlation between the horizontal and vertical distances between a pair of particles. 2DF, as shown in Fig. 7, evidently suggests that $C_{12}(h) > 0$ for all the cases and for all the levels, h. The symmetry of $C_{ij}(h)$ allows two real eigenvalues, $\lambda_1(h)$ and $\lambda_2(h) (< \lambda_1(h))$, and the corresponding eigenvectors. The direction of the eigenvector corresponding to $\lambda_1(h)$ indicates the direction along which the relative distance between a pair of particles has the maximum variance, λ_1, for a group of particle pairs satisfying the inequality in Eq. (17). $\lambda_1(h)$ is a monotonically decreasing function of h, because as h approaches $g(0, 0)$, the maximum value is $g(x, y)$ found at the origin and the corresponding cluster of particles becomes smaller, as shown in Fig. 8. However, as h decreases to 1, the cluster of particles becomes larger. In Fig. 8, $\sqrt{\lambda_1(h)}/\eta$ and $\sqrt{\lambda_2(h)}/\eta$ are plotted for the range $1.06 < h < g_{max}$. It is noticeable that in the absence of gravity, as h approaches g_{max}, the difference between $\lambda_1(h)$ and $\lambda_2(h)$ reduces; however, it never goes to zero, implying that small-scale clustering maintains anisotropy, consistent with a previous observation by Gualtieri *et al.* [45]. More importantly, as the gravity factor increases, this anisotropy becomes stronger.

We also investigated the orientation of clusters of different scales by monitoring the direction of the corresponding eigenvector. The angle formed between the principal direction of $\lambda_1(h)$ and the horizontal direction is defined as $\theta(h)$. Figures 8(b), 8(d), 8(f), and 8(h) show the principal angle of particle clustering $\theta(h)$ as a function of $\sqrt{\lambda_1(h)}/\eta$ for various Stokes numbers. The limiting angle as $\sqrt{\lambda_1(h)}/\eta$ approaches 1 is the angle of the smallest scale of clustering. In comparison, the angle at the maximum $\sqrt{\lambda_1(h = 1.06)}/\eta$ corresponds to the angle of the large-scale clustering. The behavior of $\lambda_1(h)$ and $\theta(h)$ for St = 0.1 is not shown, because the clustering is not recognized well. In the absence of gravity, angle $\theta(h)$ increases with a scale for St = 0.5 and 1, whereas the angle shows a local minimum in the intermediate scale. However, in the presence of gravity the behavior of the angle is quite diverse, depending on the strength of gravity and scales.
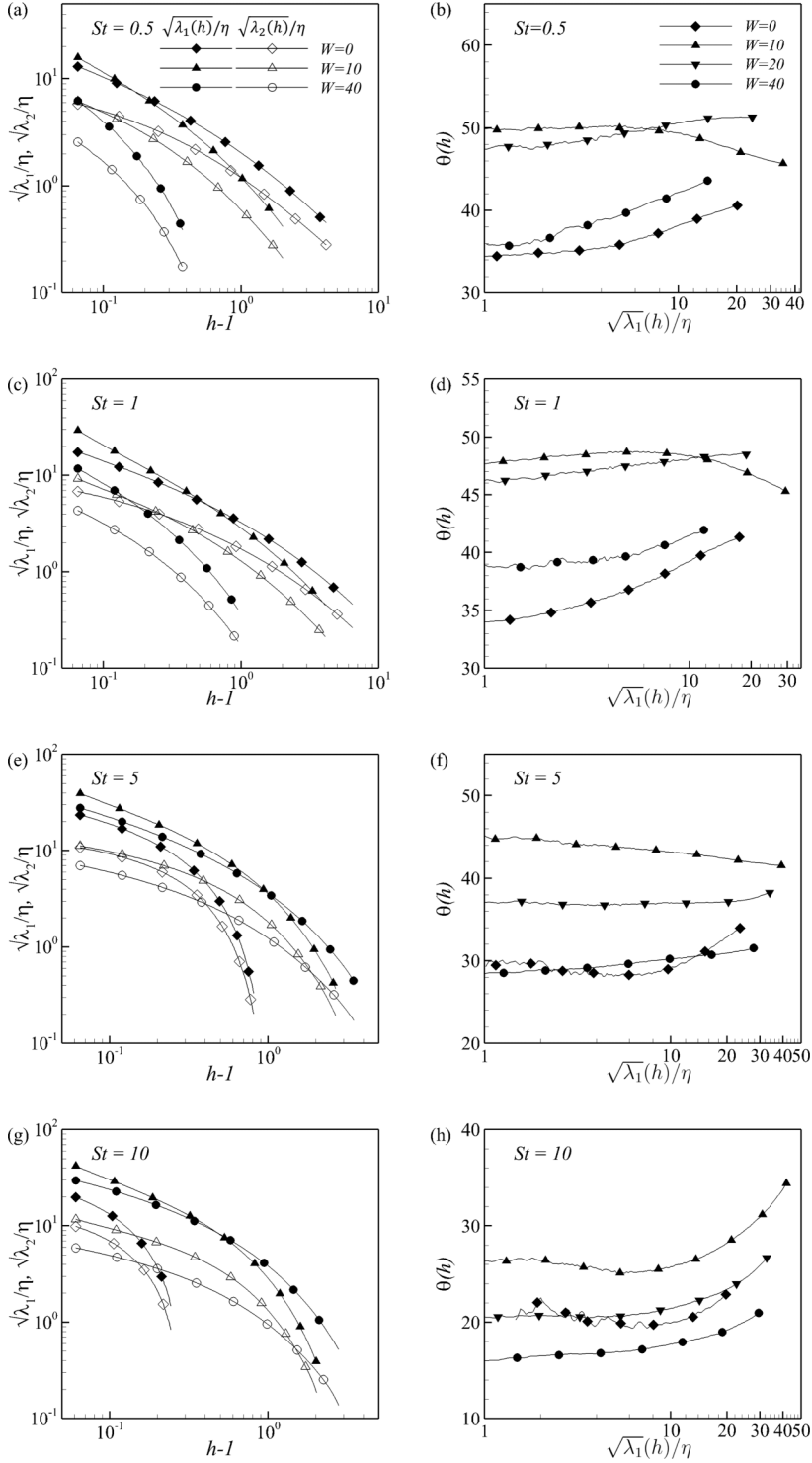
FIG. 8. Plots of $\sqrt{\lambda_1(h)}$ and $\sqrt{\lambda_2(h)}$ [(a), (c), (e), and (g)] and principal angles of particle distributions [(b), (d), (f), and (h)] as a function of $\sqrt{\lambda_1}$, normalized by Kolmogorov scale, η for various gravity factors, $W = 0, 10, 20, 40$ and St = 0.5, 1, 5, 10.
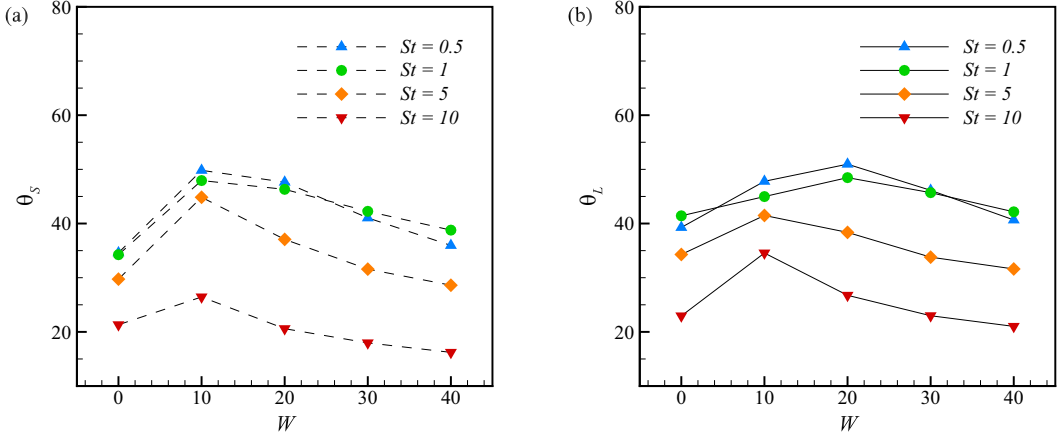
FIG. 9. Principal angles of (a) small-scale distribution and (b) large-scale distribution vs gravity factor for St $= 0.1, 0.5, 1, 5,$ and 10.

In Fig. 9 the limiting angles at both the extreme scales denoted by θ_S as $\sqrt{\lambda_1(h)}/\eta \to 1$ ($h \to g_{max}$) and θ_L as $\sqrt{\lambda_1(h)}/\eta \to$ are maximum, as presented for various Stokes numbers and gravity factors. θ_S shows the maximum at $W = 10$ for all the Stokes numbers, whereas θ_L shows the maximum at $W = 20$ for St $= 0.5$ and 1 and at $W = 10$ for St $= 5$ and 10. Both the angles tend to decrease as the gravity factor increases, implying that the structure of the cluster prefers horizontal stretching.

D. Multifractal nature of small-scale clustering

As discussed using 2DF in the previous section, the localization of the particles of small scales results in an increase in the particle density. The density of particles is singular, and its pair correlation function or 2DF shows a power-law divergence $r^{-\alpha}$ at a small separation r, where α is the so-called correlation codimension. In this section we discuss the investigation of whether such a multifractal scaling holds in the small-scaling cluster of settling particles in shear turbulence. Particularly, we discuss the behavior of 2DF for a small separation r.

Gualtieri *et al.* [45] found that the statistics of the suspended particles in the shear turbulence exhibit the same results as that in the isotropic flow. They expressed the ADF as an angle-dependent RDF $g(r, \hat{r}_i)$, where $r = |r_i|$, and $\hat{r}_i$ is the unit-directional vector of the distance vector r_i. Using spherical harmonics decomposition, multifractal scaling was investigated. In our other study [65] the angle-dependent RDF and its multifractal nature were examined for settling droplets in the isotropic turbulence. In a previous study the angle-dependent RDF, $g(r, \phi)$, was defined to determine a pair of droplets at a given distance r and polar angle ϕ (the z axis was directed upward). Column-shaped particle clustering at a small Fr($= $ St$/W$) discovered by Bec *et al.* [13], Park and Lee [14] was analyzed by assuming that the multifractality is confined in the horizontal direction. Therefore $g(r, \phi)$ depends only on the horizontal separation $r \sin \phi$, where the multifractality dictates the power-law dependence $(r \sin \phi)^{-\alpha}$:

$$g(r, \phi) = \left(\frac{l_c}{r \sin \phi} \right)^{\alpha}, \quad r < l_c, \quad \phi > \phi^*, \tag{18}$$

where l_c is the cut-off scale approximately ten times larger than the Kolmogorov scale ($l_c \sim 10\eta$), and the critical angle ϕ^* is considerably smaller than 1 ($\phi^* \ll 1$). α is twice the information codimension as given by the Kaplan-Yorke formula.
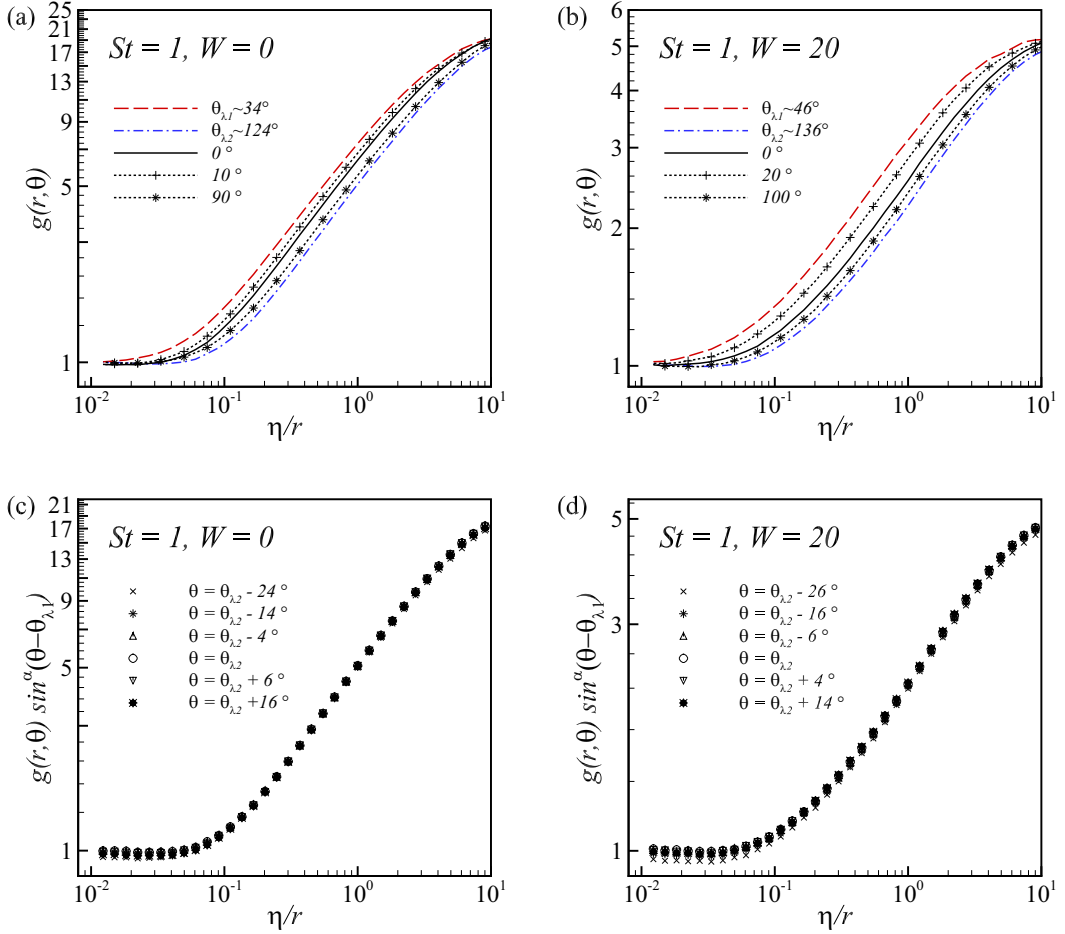
FIG. 10. Plots of $g(r, \theta)$ [(a) and (b)] and the compensated RDF $g(r, \theta) \sin^\alpha(\theta - \theta_{\lambda_1})$ [(c) and (d)] vs η/r at representative angles θ in case of (a), (c) $St = 1, W = 0$, and (b), (d) $St = 1, W = 20$. Red dashed line represents the most stretching principal angle θ_S for θ_{λ_1}, and blue dotted line represents the most compressive principal angle for θ_{λ_2}.

Here we investigate the extension of the behavior of the angle-dependent RDF to small-scale clustering of settling particles in the shear turbulence. For this purpose the angle-dependent property of the 2DF introduced in the previous section is expressed using the polar coordinate $g(x, y) = g(r, \theta)$, where $r = \sqrt{x^2 + y^2}$ and $\theta = \tan^{-1} x/y$, which is the angle from the horizontal direction. $g(r, \theta)$ is obtained from $g(x, y)$, as depicted in Fig. 7 at $d\theta = 10°$ intervals for the range of $0° \leqslant \theta \leqslant 180°$ by using a bilinear interpolation. In Figs. 10(a) and 10(b), $g(r, \theta)$ are drawn for several choices of θ for $St = 1$ and $W = 0$ and 20. Here the red dashed line and the blue dotted line indicate $g(r, \theta_{\lambda_1})$ and $g(r, \theta_{\lambda_2})$, where $\theta_{\lambda_1} = \theta_S$ in Fig. 9, which is the angle between the most stretching direction of the smallest-scale clustering and the horizontal direction. $\theta_{\lambda_2} = \theta_S + 90°$. Obviously, $g(r, \theta)$ decays most rapidly as r increases when $\theta = \theta_{\lambda_2}$, i.e., in the most compressive direction, whereas $g(r, \theta)$ decreases most gradually when $\theta = \theta_{\lambda_1}$, in the most stretching direction. $g(r, \theta)$ for other angles is found to be between them. Note that the slope of the $g(r, \theta)$ for the range of $0.2 \leqslant \eta/r \leqslant 2$ is established at all the angles, clearly suggesting a divergent behavior, $g(r, \theta) \sim r^{-\alpha}$ as $r \to 0$.

For the settling droplets in an isotropic turbulence, as discussed by Fouxon et al. [65], the angle-dependent RDF $g(r, \phi)$ at $\phi = 0$ (vertical direction) decreases most slowly in r, and $g(r, \phi)$ at

TABLE IV. Correlation codimension α for St $= 0.5$ and 1, and $W = 0, 10, 20, 30$, and 40. Fr $=$ St$/W$.

			α		
St	W	Fr	Shear turbulence (Present)	Isotropic turbulence (Fouxon *et al.* [65])	Isotropic turbulence (Bec *et al.* [13,69])
0.1	0	∞	–	–	0.12
0.5	0	∞	0.636	–	0.68
0.5	10	0.05	0.374	–	–
0.5	20	0.025	0.224	–	–
0.5	30	0.0167	0.142	–	–
0.5	40	0.0125	0.096	–	–
1	0	∞	0.706	–	0.63
1	10	0.1	0.540	–	–
1	20	0.05	0.440	0.588	0.58
1	30	0.033	0.318	0.478	–
1	40	0.025	0.236	0.363	–

$\phi = 90°$ (horizontal direction) decays most rapidly in r. In shear turbulence, the most stretching direction of the particle cluster is found in the θ_{λ_1} direction, suggesting that the combined effect of gravity and shear creates the effective gravity in this most stretching direction. Therefore we propose to extend Eq. (18) to shear turbulence by expressing $g(r, \theta)$ by

$$g(r, \theta) = \left(\frac{l_c}{r \sin (\theta - \theta_{\lambda_1})} \right)^\alpha, \quad r < l_c, \quad \theta - \theta_{\lambda_1} > \theta^*, \tag{19}$$

where l_c is the cut-off length scale and θ^* is the critical angle. It is found in our study that $l_c = 6\eta \sim 10\eta$ and $\theta^* \sim 0.5$. As demonstrated in Figs. 10(c) and 10(d) for St $= 1$ and $W = 0$ and 20, the compensated RDF, $g(r, \theta) \sin^\alpha(\theta - \theta_{\lambda_1})$, for various angles collapses to a single curve, validating Eq. (19). Here α is determined by the method described below.

Following this, we attempted to estimate the correlation codimension α, which is known to be related with twice the Kaplan-Yorke codimension, C_{KY} [14,66]. This leads to a relation with the correlation dimension $\mathcal{D}_2$, a multifractal measure associated with the particle density correlation [67,68]; $\mathcal{D}_2 = 3 - \alpha = 3 - 2C_{KY}$. By definition, $C_{KY} = |\Sigma \Lambda_i|/|\Lambda_3| \ll 1$ at a low compressibility [14,66]. Λ_i indicates the Lyapunov exponent, which can be computed by tracking numerous pairs of particles. We conducted separate real-time simulations to estimate the Lyapunov exponents. The initial distance between the particles is set as $1/100\,000$th of the Kolmogorov length scale. After the transient period due to an arbitrary initial condition for the particle velocity, the changes in the distance between two particles, of the area between three particles, and of the volume constructed from four particles are monitored based on the Gram-Schmidt renormalization for a period of $43\tau_\eta$. The 10 000 sets of pairs are released in one field, and the data are collected over a total of 77 flow fields.

The obtained correlation codimensions for St $= 0.5$ and 1, compared to the results for isotropic turbulence by Bec *et al.* [13,69] and Fouxon *et al.* [65], are listed in Table IV. The RDFs in the steepest direction, $g(r, \theta_{\lambda_2})$ for St $= 0.1, 0.5, 1$, and 5, are plotted in Fig. 11 and compared with the scaling estimation of $(l_c/r)^\alpha$, with the corresponding α listed in Table IV. In the absence of gravity ($W = 0$), the values of α for shear turbulence and for isotropic turbulence at St $= 0.5$ are comparable, whereas α for St $= 1$ shows some discrepancy between the shear turbulence and the isotropic turbulence, as seen in Table IV. As W increases, α for the shear turbulence decreases more rapidly than that for the isotropic turbulence. When St $= 0.1$, in the absence of gravity the slope of $g(r, \theta_{\lambda_2})$ is captured well by the value of α for isotropic turbulence estimated in Bec *et al.* [69]. A similar universal behavior in the absence of gravity was observed by Gualtieri *et al.* [45];
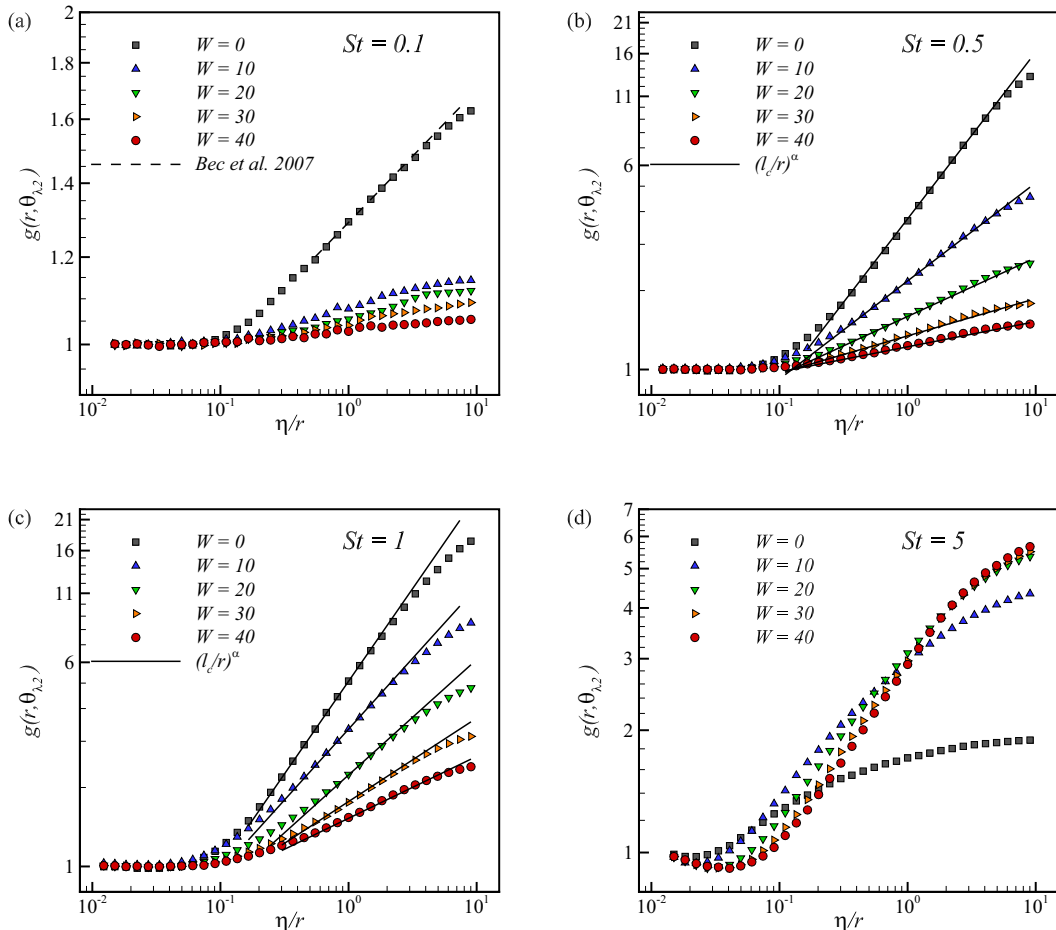
FIG. 11. Plots of $g(r, \theta_{\lambda_2})$ for St = 0.1, 0.5, 1, and 5 and St = 0.1. The RDF for $W = 0$ is approximated by $(l_c/r)^\alpha$ well with the value of α in the isotropic turbulence, given by Bec *et al.* [69]. For St = 0.5 and 1, in most cases, the diverging behavior of $g(r, \theta)$ as $r \to 0$ is remarkably fitted well by $(l_c/r)^\alpha$ with the corresponding α listed in Table IV. For St = 5, the diverging behavior is not observed.

thus gravity causes some differences in the diverging behavior. As shown in Figs. 3 and 7, small-scale clustering is weakened with gravity for St $\leqslant$ 1. Figure 11 clearly shows that settling particles in shear turbulence exhibit the multifractal nature in small-scale clustering, by demonstrating the divergent behavior and slope. Such a diverging behavior is partially observable under strong gravity when St = 5, as shown in Fig. 11(d).

IV. CONCLUSIONS

In this study we investigated the clustering behavior of settling particles in homogeneous shear turbulence by direct numerical simulation with a point-particle approximation for small spherical particles with a diameter smaller than the Kolmogorov length scale. The ranges of the Stokes number and gravity factor are St = 0.1, 0.5, 1, 5, and 10 and $W = 0$, 10, 20, 30, and 40. To investigate the long-term behavior of particles, a homogeneous shear turbulence in a confined box was simulated by the combined usage of the algorithm by Brucker *et al.* [51] and the remeshing model by Rogallo [53].

The mean statistics of particle motion, such as the mean settling velocity, mean horizontal slip velocity, and mean trajectory of the particles, were obtained. For the range of the gravity factor considered in this study, the enhancement of the settling velocity is not highly pronounced, and the mean horizontal slip velocity of the particles relative to the mean shear is insignificant. Therefore the mean trajectory of the particles did not show noticeable deviation from the trajectory of a particle in the turbulence-free shear flow. However, the particle dispersion relative to the mean trajectory exhibited a ballistic-to-diffusion transition with a subsequent shear-diffusion behavior depending on the Stokes number.

The clustering behavior of the settling particles was investigated by various measures. In the absence of gravity, the strongest clustering of particles was observed at $St = 1$. However, as the gravity factor increases, the clustering at $St = 1$ becomes weaker and a new type of clustering emerges for $St = 5$ and 10. This is similar to that found by Park and Lee [14] in their simulation of the settling particles in a homogeneous isotropic turbulence. Specifically, a new type of clustering for $St > 1$ is observed as the gravity factor increases. The quantitative analysis by measuring the averaged distance to the closest particle supports the clustering behavior.

A unique feature of the clustering observed in shear turbulence is that the clusters show a preferential direction owing to the combined effect of shear and gravity. To quantify this behavior, we introduced and measured a two-dimensional distribution function of the particles, $g(x, y)$. By applying principal component analysis to it, we could identify the preferential direction of clusters at different scales. As St and W increase, the clusters tend to align more with the horizontal direction. These particle clusters suggest that both the sweep-stick mechanism at high Stokes numbers and the large-scale preferential sweeping of settling particle for low Fr were affected by shear.

Finally, multifractal characteristics of small-scale clusters were investigated. From the principal component analysis of $g(x, y)$, we could identify the direction of the most clustering at small scales. Subsequently, as r approached zero for isotropic turbulence, the diverging behavior of the RDF, $g(r) \sim r^{-\alpha}$, was extended to anisotropic clusters, and a similar diverging behavior could be observed near the most clustering direction. Therefore the two-dimensional distribution function can be expressed in the polar form, $g(r, \theta) \sim r^{-\alpha} \sin^{-\alpha}(\theta - \theta_{\lambda_1})$. An estimation of the correlation codimension α was made by measuring the Kaplan-Yorke codimension. We numerically confirmed this angle-dependent diverging behavior for $St \leqslant 1$.

---

[1] G. Falkovich, A. Fouxon, and M. G. Stepanov, Acceleration of rain initiation by cloud turbulence, Nature (London) **419**, 151 (2002).

[2] K. D. Squires and J. K. Eaton, Preferential concentration of particles by turbulence, Phys. Fluids A **3**, 1169 (1991).

[3] G. F. Froment, K. B. Bischoff, and J. De Wilde, *Chemical Reactor Analysis and Design* (Wiley, New York, 1990), Vol. 2.

[4] L. Guzzella and C. Onder, *Introduction to Modeling and Control of Internal Combustion Engine Systems* (Springer Science & Business Media, New York, 2009).

[5] M. R. Maxey, The gravitational settling of aerosol particles in homogeneous turbulence and random flow fields, J. Fluid Mech. **174**, 441 (1987).

[6] W. C. Reade and L. R. Collins, Effect of preferential concentration on turbulent collision rates, Phys. Fluids **12**, 2530 (2000).

[7] S. Balachandar and J. K. Eaton, Turbulent dispersed multiphase flow, Annu. Rev. Fluid Mech. **42**, 111 (2010).

[8] R. Monchaux, M. Bourgoin, and A. Cartellier, Analyzing preferential concentration and clustering of inertial particles in turbulence, Int. J. Multiphase Flow **40**, 1 (2012).

[9] W. W. Grabowski and L.-P. Wang, Growth of cloud droplets in a turbulent environment, Annu. Rev. Fluid Mech. **45**, 293 (2013).

[10] S. Goto and J. C. Vassilicos, Self-similar clustering of inertial particles and zero-acceleration points in fully developed two-dimensional turbulence, Phys. Fluids **18**, 115103 (2006).

[11] L. Chen, S. Goto, and J. Vassilicos, Turbulent clustering of stagnation points and inertial particles, J. Fluid Mech. **553**, 143 (2006).

[12] S. Goto and J. C. Vassilicos, Sweep-Stick Mechanism of Heavy Particle Clustering in Fluid Turbulence, Phys. Rev. Lett. **100**, 054503 (2008).

[13] J. Bec, H. Homann, and S. S. Ray, Gravity-Driven Enhancement of Heavy Particle Clustering in Turbulent Flow, Phys. Rev. Lett. **112**, 184501 (2014).

[14] Y. Park and C. Lee, Gravity-driven clustering of inertial particles in turbulence, Phys. Rev. E **89**, 061004(R) (2014).

[15] O. Ayala, B. Rosa, L.-P. Wang, and W. W. Grabowski, Effects of turbulence on the geometric collision rate of sedimenting droplets. Part 1. Results from direct numerical simulation, New J. Phys. **10**, 075015 (2008).

[16] R. A. Shaw, Particle-turbulence interactions in atmospheric clouds, Annu. Rev. Fluid Mech. **35**, 183 (2003).

[17] R. Onishi, K. Takahashi, and S. Komori, Influence of gravity on collisions of monodispersed droplets in homogeneous isotropic turbulence, Phys. Fluids **21**, 125108 (2009).

[18] I. Fouxon, Y. Park, R. Harduf, and C. Lee, Inhomogeneous distribution of water droplets in cloud turbulence, Phys. Rev. E **92**, 033001 (2015).

[19] M. R. Maxey and J. J. Riley, Equation of motion for a small rigid sphere in a nonuniform flow, Phys. Fluids **26**, 883 (1983).

[20] D. Modarress, S. Elghobashi, and H. Tan, Two-component LDA measurement in a two-phase turbulent jet, AIAA J. **22**, 624 (1984).

[21] E. K. Longmire and J. K. Eaton, Structure of a particle-laden round jet, J. Fluid Mech. **236**, 217 (1992).

[22] J. R. Fessler, J. D. Kulick, and J. K. Eaton, Preferential concentration of heavy particles in a turbulent channel flow, Phys. Fluids **6**, 3742 (1994).

[23] D. Kaftori, G. Hetsroni, and S. Banerjee, Particle behavior in the turbulent boundary layer. I. Motion, deposition, and entrainment, Phys. Fluids **7**, 1095 (1995).

[24] M. Righetti and G. P. Romano, Particle–fluid interactions in a plane near-wall turbulent flow, J. Fluid Mech. **505**, 93 (2004).

[25] J. N. Chung and T. R. Troutt, Simulation of particle dispersion in an axisymmetric jet, J. Fluid Mech. **186**, 199 (1988).

[26] L. Tang, F. Wen, Y. Yang, C. T. Crowe, J. N. Chung, and T. R. Troutt, Self-organizing particle dispersion mechanism in a plane wake, Phys. Fluids A **4**, 2244 (1992).

[27] J. Lee and C. Lee, Modification of particle-laden near-wall turbulence: Effect of Stokes number, Phys. Fluids **27**, 023303 (2015).

[28] M. R. Maxey, The motion of small spherical particles in a cellular flow field, Phys. Fluids **30**, 1915 (1987).

[29] C. Marchioli, M. Picciotto, and A. Soldati, Influence of gravity and lift on particle velocity statistics and transfer rates in turbulent vertical channel flow, Int. J. Multiphase Flow **33**, 227 (2007).

[30] V. Lavezzo, A. Soldati, S. Gerashchenko, Z. Warhaft, and L. R. Collins, On the role of gravity and shear on inertial particle accelerations in near-wall turbulence, J. Fluid Mech. **658**, 229 (2010).

[31] J. Lee and C. Lee, The effect of wall-normal gravity on particle-laden near-wall turbulence, J. Fluid Mech. **873**, 475 (2019).

[32] W. G. Rose, Results of an attempt to generate a homogeneous turbulent shear flow, J. Fluid Mech. **25**, 97 (1966).

[33] F. H. Champagne, V. G. Harris, and S. Corrsin, Experiments on nearly homogeneous turbulent shear flow, J. Fluid Mech. **41**, 81 (1970).

[34] P. J. Mulhearn and R. E. Luxton, The development of turbulence structure in a uniform shear flow, J. Fluid Mech. **68**, 577 (1975).

[35] S. Tavoularis and S. Corrsin, Experiments in nearly homogeneous turbulent shear flow with a uniform mean temperature gradient. Part 1, J. Fluid Mech. **104**, 311 (1981).

[36] S. Tavoularis and S. Corrsin, Experiments in nearly homogeneous turbulent shear flow with a uniform mean temperature gradient. Part 2. The fine structure, J. Fluid Mech. **104**, 349 (1981).

[37] M. M. Rogers and P. Moin, The structure of the vorticity field in homogeneous turbulent flows, J. Fluid Mech. **176**, 33 (1987).

[38] R. J. Adrian and P. Moin, Stochastic estimation of organized turbulent structure: Homogeneous shear flow, J. Fluid Mech. **190**, 531 (1988).

[39] M. J. Lee, J. Kim, and P. Moin, Structure of turbulence at high shear rate, J. Fluid Mech. **216**, 561 (1990).

[40] S. Kida and M. Tanaka, Dynamics of vortical structures in a homogeneous shear flow, J. Fluid Mech. **274**, 43 (1994).

[41] A. Pumir, Turbulence in homogeneous shear flows, Phys. Fluids **8**, 3112 (1996).

[42] X. Shen and Z. Warhaft, The anisotropy of the small scale structure in high Reynolds number ($R_\lambda \sim 1000$) turbulent shear flow, Phys. Fluids **12**, 2976 (2000).

[43] A. M. Ahmed and S. Elghobashi, Direct numerical simulation of particle dispersion in homogeneous turbulent shear flows, Phys. Fluids **13**, 3346 (2001).

[44] B. Shotorban and S. Balachandar, Particle concentration in homogeneous shear turbulence simulated via Lagrangian and equilibrium Eulerian approaches, Phys. Fluids **18**, 065105 (2006).

[45] P. Gualtieri, F. Picano, and C. M. Casciola, Anisotropic clustering of inertial particles in homogeneous shear flow, J. Fluid Mech. **629**, 25 (2009).

[46] A. M. Ahmed and S. Elghobashi, On the mechanisms of modifying the structure of turbulent homogeneous shear flows by dispersed particles, Phys. Fluids **12**, 2906 (2000).

[47] M. Tanaka, Y. Maeda, and Y. Hagiwara, Turbulence modification in a homogeneous turbulent shear flow laden with small heavy particles, Int. J. Heat Fluid Flow **23**, 615 (2002).

[48] P. Gualtieri, F. Picano, G. Sardina, and C. M. Casciola, Clustering and turbulence modulation in particle-laden shear flows, J. Fluid Mech. **715**, 134 (2013).

[49] L.-P. Wang and M. R. Maxey, Settling velocity and concentration distribution of heavy particles in homogeneous isotropic turbulence, J. Fluid Mech. **256**, 27 (1993).

[50] J. Tom and A. D. Bragg, Multiscale preferential sweeping of particles settling in turbulence, J. Fluid Mech. **871**, 244 (2019).

[51] K. A. Brucker, J. C. Isaza, T. Vaithianathan, and L. R. Collins, Efficient algorithm for simulating homogeneous turbulent shear flow without remeshing, J. Comput. Phys. **225**, 20 (2007).

[52] J. Jiménez, Simulation of homogeneous and inhomogeneous shear turbulence, CTR Annual Research Briefs 2007, Stanford University, 367 (2007).

[53] R. S. Rogallo, Numerical experiments in homogeneous turbulence, NASA Technical Memorandum 81315 (1981).

[54] C. Lee, K. Yeo, and J.-I. Choi, Intermittent Nature of Acceleration in Near Wall Turbulence, Phys. Rev. Lett. **92**, 144502 (2004).

[55] J.-I. Choi, K. Yeo, and C. Lee, Lagrangian statistics in turbulent channel flow, Phys. Fluids **16**, 779 (2004).

[56] P. J. Ireland, T. Vaithianathan, P. S. Sukheswalla, B. Ray, and L. R. Collins, Highly parallel particle-laden flow solver for turbulence research, Comput. Fluids **76**, 170 (2013).

[57] A. H. Abdelsamie and C. Lee, Decaying versus stationary turbulence in particle-laden isotropic turbulence: Turbulence modulation mechanism, Phys. Fluids **24**, 015106 (2012).

[58] A. H. Abdelsamie and C. Lee, Decaying versus stationary turbulence in particle-laden isotropic turbulence: Heavy particle statistics modifications, Phys. Fluids **25**, 033303 (2013).

[59] P. J. Ireland, A. D. Bragg, and L. R. Collins, The effect of Reynolds number on inertial particle dynamics in isotropic turbulence. Part 2. Simulations with gravitational effects, J. Fluid Mech. **796**, 659 (2016).

[60] S. Corrsin, Progress report on some turbulent diffusion research, Adv. Geophys. **6**, 161 (1959).

[61] R. Monchaux, M. Bourgoin, and A. Cartellier, Preferential concentration of heavy particles: A Voronoï analysis, Phys. Fluids **22**, 103304 (2010).

[62] M. Obligado, T. Teitelbaum, A. Cartellier, P. Mininni, and M. Bourgoin, Preferential concentration of heavy particles in turbulence, J. Turbulence **15**, 293 (2014).

[63] R. Monchaux and A. Dejoan, Settling velocity and preferential concentration of heavy particles under two-way coupling effects in homogeneous turbulence, Phys. Rev. Fluids **2**, 104302 (2017).

[64] I. Jolliffe, *Principal Component Analysis* (Springer, New York, 2011).

[65] I. Fouxon, S. Lee, and C. Lee, Impacts of turbulence intermittency and sedimentation on droplet collisions in clouds, Phys. Rev. Fluids (to be published) (2020).

[66] I. Fouxon, Distribution of Particles and Bubbles in Turbulence at a Small Stokes Number, Phys. Rev. Lett. **108**, 134502 (2012).

[67] H. Hentschel and I. Procaccia, The infinite number of generalized dimensions of fractals and strange attractors, Physica D **8**, 435 (1983).

[68] P. Grassberger and I. Procaccia, Characterization of Strange Attractors, Phys. Rev. Lett. **50**, 346 (1983).

[69] J. Bec, L. Biferale, M. Cencini, A. Lanotte, S. Musacchio, and F. Toschi, Heavy Particle Concentration in Turbulence at Dissipative and Inertial Scales, Phys. Rev. Lett. **98**, 084502 (2007).